nature energy

Article

https://doi.org/10.1038/s41560-026-01989-9

Electrified reversible surface mineralization of CO_2 for direct air capture

Received: 14 March 2025

Accepted: 20 January 2026

Published online: 13 February 2026

Check for updates

Zeyan Liu[1,2,7], Huajie Ze[1,2,7], Bosi Peng[1,2,7], Charles B. Musgrave III[1,2,3], Mohammad K. Shehab[1,4], Hyun Seung Jung[1,2], Hengzhou Liu[1,2], Kent O. Kirlikovali[1,4], William A. Goddard III[3], Omar K. Farha[1,4,5,6], Ke Xie[1,2] ✉ & Edward H. Sargent[1,2,6] ✉

Electrified CO_2 capture and release from air offers net-negative emissions, but today's liquid-carbonate-based systems have a high energy cost (6–10 GJ per ton of CO_2), and organic sorbents are oxygen sensitive. Here we report electrified CO_2 surface mineralization/demineralization capture/release, wherein an inorganic capture sorbent, MnO_2, is electrochemically reduced/activated to generate Mn(III), which mineralizes CO_2 to form $MnOOCO_2H$ (operando Raman); the process is reversed under oxidative potential. This approach is built upon Mn redox reaction that resides within the water-stable bracket, offering tunable driving force (kinetics/productivity) with applied potential (energy). After optimizing the electrochemical protocol, we capture from air (0.04% CO_2 and 21% O_2) at 4.1 GJ per ton of CO_2, with capacity and kinetics comparable to prior sorbents, low sensitivity to oxygen/humidity, 80% single-pass CO_2 capture ratio and release under a pure CO_2 carrier gas stream and pressure drop <150 Pa. The system operates >1,000 h with >90% capacity retention and scales to 20 cm^2 without loss; remaining challenges include material utilization, electrolyte, gas flow/pressure drop and CO_2-purity management.

Direct air capture (DAC) has the potential to contribute to net-zero goals by offsetting hard-to-abate emissions[1,2]. Key priorities for DAC include lowering energy consumption to well below 10 GJ per ton of CO_2 (ton_{CO2}); powering the process using low-carbon-intensity electricity[3–7] and enabling capture from input air with substantial partial pressures of both oxygen and humidity.

Electrified carbon capture technologies using pH-swing devices[4,5,8–10] (Fig. 1a) have shown promise in DAC, but these are bounded by a typical minimum energy cost of ~3.6 GJ per ton_{CO2}, since a Nernst potential difference of 0.83 V arises due to the large pH gradient at membrane interfaces for acceptable capture and release kinetics (> 5 mA cm^{-2}) (ref. 11). This bound arises from the pH required (pH ~14) for the capture of carbon dioxide (CO_2) and the low pH (pH ~0) required for CO_2 release from the aqueous capture liquid and the minimum of two electrons per CO_2 mandated by the need to effect the shift first from carbonate to bicarbonate, and thence from bicarbonate to $CO_{2(g)}$. The empirical energy expended in experimentally implemented systems processing post-capture liquids has to date been in the range of 2.5× to 5× this value[5].

In contrast, reversible CO_2 adsorption devices (Fig. 1b) that employ redox-active sorbents, such as quinone-based organic nucleophiles, are capable of capturing CO_2 via a one-electron process, and the CO_2 capture and release driving force is progressively controlled (tuned) across the redox window (redox gap) of the sorbent, allowing a voltage

[1]Department of Chemistry, Northwestern University, Evanston, IL, USA. [2]Department of Electrical and Computer Engineering, Northwestern University, Evanston, IL, USA. [3]Materials and Process Simulation Center, California Institute of Technology, Pasadena, CA, USA. [4]International Institute for Nanotechnology, Northwestern University, Evanston, IL, USA. [5]Department of Chemical and Biological Engineering, Northwestern University, Evanston, IL, USA. [6]Paula M. Trienens Institute for Sustainability and Energy, Northwestern University, Evanston, IL, USA. [7]These authors contributed equally: Zeyan Liu, Huajie Ze, Bosi Peng. ✉e-mail: ke-xie@northwestern.edu; ted.sargent@northwestern.edu

https://doi.org/10.1038/s41560-026-01989-9

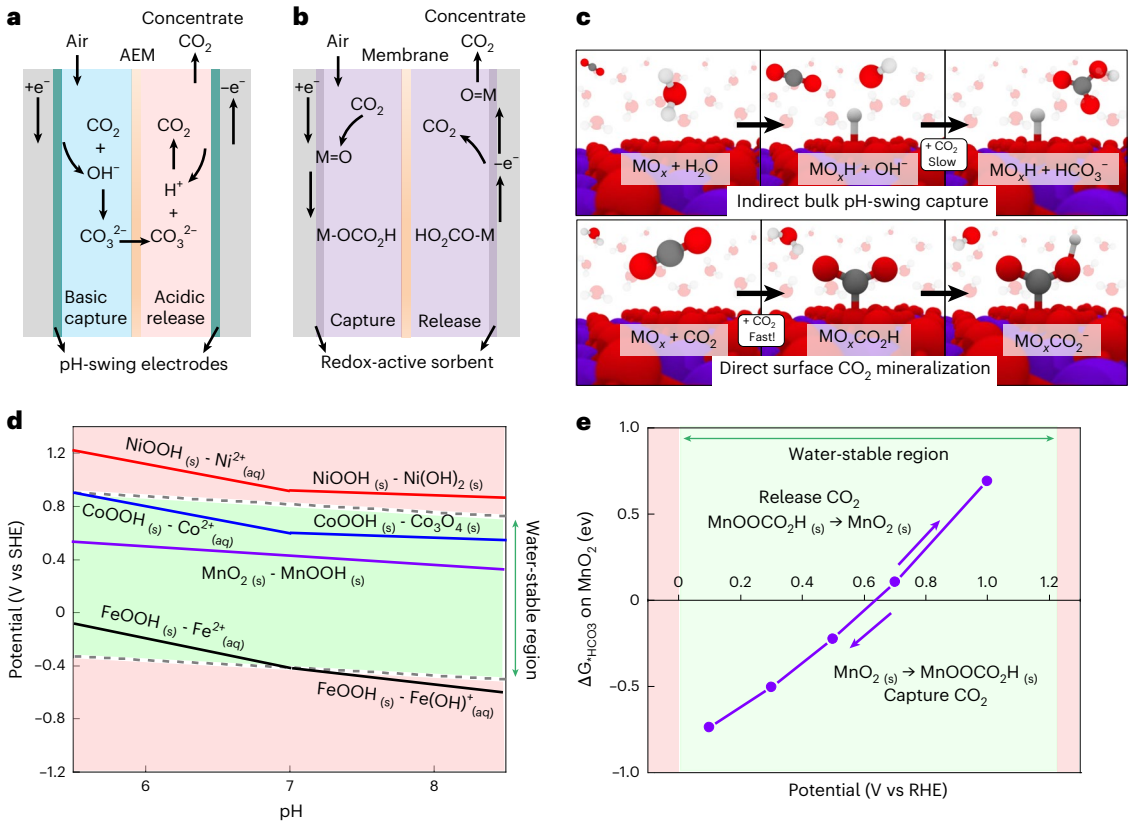

Fig. 1 | Electrified capture/release devices and chemical concepts, including eCO$_2$-sMDCR. a, Indirect, bulk-pH-swing device. **b**, Adsorption/surface mineralization device. In the indirect system, to capture CO_2 with kinetics suited for DAC, CO_2 is captured by forming CO_3^{2-}, which consumes two OH^- ions and thus requires two electrons. The reversible CO_2 adsorption/surface mineralization device can be operated in a regime employing one electron per CO_2. **c**, Surface chemistry of direct surface mineralization CO_2 capture compared to pH-swing CO_2 capture. Red: oxygen atoms, purple: metal (Mn) atoms, grey: carbon atoms, white: hydrogen atoms. **d**, Pourbaix diagram screening of a range of candidate transition metal oxides. MnO_2 avoids dissolution and has a redox window within the water-stable potential bracket at near-neutral conditions[16–19]. Data adapted from the Materials Project under a Creative Commons Attribution 4.0 License[18]. **e**, DFT calculation of the $*OCO_2H$ adsorption energy in the form of $Mn-OCO_2H$ versus potential. The crossover in free energy circa 0.7 V indicates that CO_2 capture and release are tuned using the applied potential. We use the chemical formula $MnOOCO_2H$ to denote the formation of $Mn-OCO_2H$ on the surface when MnO_2 is reduced. Illustration in **c** was generated by Ovito and the structures for calculation in **e** were generated by Vesta 3 (ref. 45).

swing lower than the Nernst minimum of 0.83 V (refs. 3,12). However, some organic implementations of redox-swing DAC systems suffer sensitivity to O_2 in air, as the low reduction potential of the organic redox mediator (for example, quinones) often leads to the formation of destructive superoxide[6,8,13].

We asked whether inorganic materials might be used in solid-state electrochemically controlled capture and release from a redox-active sorbent. We noted that at the metal–oxygen site (M–O) within metal (hydro)oxides, electroreduction has the potential to create electron-rich oxygen sites ($M-O^-$) and that these may have CO_2 capture ability. The metalloenzyme carbonic anhydrase, which with its $Zn-O^-H$ intermediate containing an electron-rich oxygen[14,15] has a CO_2 reaction rate constant that is greater than ten times that of the free hydroxide anion, provides one such precedent of high reactivity with CO_2.

Motivated by this concept, here we explore and report electrified CO_2 surface mineralization/demineralization capture/release (eCO$_2$-sMDCR) based on Mn redox couple: the MnO_2 is electrically reduced to generate Mn(III), which mineralizes with CO_2 to form $MnOOCO_2H$, and subsequent oxidation reverses the reaction to release CO_2. We construct an eCO$_2$-sMDCR device and study the electrochemical protocol and demonstrate CO_2 capture across a wide range of concentrations (0.04% to 100%), low oxygen/humidity sensitivity and good cyclic stability. We explore the path towards pilot-scale demonstration and envision remaining challenges and opportunities in electrochemical device architecture, low pressure-drop contactor design and CO_2-purity management.

Concept and mechanism

We depict in Fig. 1c the hypothesized process of direct surface mineralization of CO_2. Surface electron-rich active sites are posited to be created during electroreduction, and it is of interest to study the kinetics and energetics compared to indirect bulk-pH-swing capture.

In such eCO$_2$-sMDCR device, the electrochemical capture and release sorbent should fulfil several requirements. First, it should be redox-active in near-neutral conditions: the reduction reaction must, under these conditions, create active electron-rich oxygen at the metal oxide surface nucleophilic sites to react with CO_2. Second, to be able to operate in an aqueous system, a metal oxide should have a redox potential window that exhibits minimal overlap with the undesired side reactions of water dissociation and oxygen reduction. Finally, to ensure the stability of the capture and release electrode, the redox reactions should occur between two solid phases; in other words, the active electrode materials should not dissolve in the near-neutral conditions during the redox cycling.

We consider representative redox-active metal oxide candidates MnO_2, Co_3O_4, Fe_2O_3 and $Ni(OH)_2$ and examined their Pourbaix stability in light of these criteria (Fig. 1d)[16–19]. Density functional theory (DFT) simulations show that CO_2 capture and release are controlled by the potential at the MnO_2 surface, with the crossover (from capture to

https://doi.org/10.1038/s41560-026-01989-9

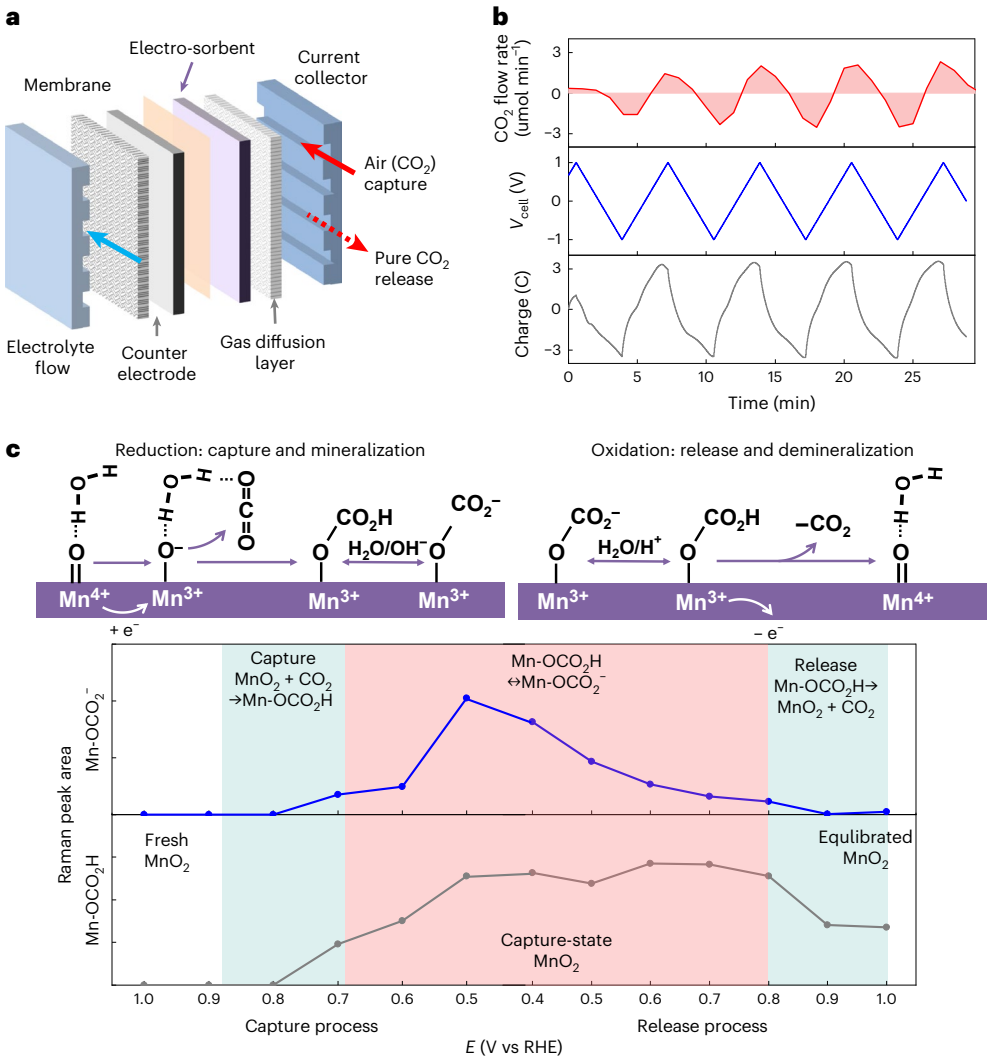

Fig. 2 | Proof-of-concept of the eCO_2-sMDCR device and mechanistic study using operando Raman spectroscopy. a, The eCO_2-sMDCR device and the proposed CO_2 reversible surface mineralization capture and release mechanism. Only the working electrode was analysed in this study. **b**, Experimental evidence of potential-dependent CO_2 capture and release. **c**, CO_2 capture from 1.0 to 0.4 V vs RHE and CO_2 release from 0.4 to 1.0 V vs. RHE, witnessed using Raman spectroscopy. In Raman, a potential-dependent increase/decrease in bicarbonate ($Mn–OCO_2H$) and then carbonate ($Mn–OCO_2^-$) peaks are observed during capture/release.

release) potential residing within the water-stable potential region near 0.65 V vs RHE (Fig. 1e).

It is seen in Fig. 1e that the driving force for capture or release is potential-dependent in the redox-active sorbent system, that is, it increases in amplitude as a higher potential is applied. This can be of use when tuning the applied potential window to different scenarios, such as point source versus direct air capture. In contrast, many prior sorbent-based strategies for CO_2 capture are determined by an intrinsic/pre-ordained CO_2 binding strength, and it is thus not possible to fine-tune adsorption kinetics and release/regeneration energy[20].

To study capture and release, both using MnO_2 and control metal oxides, we developed a membrane-electrode-assembly system in which the metal oxide electro-sorbent was coated on both sides of the membrane: a symmetric eCO_2-sMDCR device (Fig. 2a). We apply a negative (reducing) potential to begin the CO_2 capture phase and later switch the cell voltage to an oxidative potential for CO_2 release.

As in prior bench-scale analyses[3,10,21–24], we use a CO_2 analyser (Supplementary Fig. 1a) and a continuous flow carrier gas to quantify the capture and release of CO_2. We note that the energy costs reported here are those associated with electrochemical capture and release event; in future implemented systems, energy costs associated with processes such as vacuum pumping and compression will also be important. We discuss and include these in the techno-economic analysis herein (Supplementary Notes 1 and Methods)[25].

The pH of the electrolyte was monitored and, through the use of a mixed Na_2SO_4 and Na_2HPO_4 solution (total Na^+ concentration of 1 M), was buffered, residing at ~ pH 7 to minimize the impact of pH fluctuations on CO_2 capture and release.

We first studied capture from pure CO_2 in the inlet stream. When we scanned the cell voltage using cyclic voltammetry between −1 V to 1 V, we observed a voltage-dependent pressure swing, where scanning towards an oxidative potential of 1 V led to a pressure increase and scanning towards a reduction potential of −1 V led to a decrease (Supplementary Fig. 1b). Control experiments, including using pure N_2 as feed gas (Supplementary Fig. 1c) and also using only carbon paper as the electrode (Supplementary Fig. 1d), each showed no voltage-dependent pressure swing. This suggests that possible side reactions, such as oxygen reduction reaction during reductive capture and the oxygen evolution and carbon oxidation reactions during oxidative release, are not dominant.

We then used a CO_2 analyser to measure CO_2 capture and release directly (Fig. 2b), finding that the reductive scan led to decreased CO_2

concentration (capture) in the outlet stream and the oxidative scan led to increased CO_2 concentration in the outlet gas stream (release). The impact of possible CO_2 capture with aqueous electrolyte was also examined and found to be minimal (Supplementary Fig. 1e).

Quantitatively, we monitored the CO_2 capture and release rate based on the CO_2 analyser response (Supplementary Fig. 2 and Methods), finding that increasing the current from 1 to 4 mA cm^{-2} led to an increase in the CO_2 capture and release rate from 3 to 10 μmol min^{-1} (Supplementary Fig. 2a). Over this range, the capture rate increased linearly with the charging rate (Supplementary Fig. 2b). The Coulombic efficiency and energy cost of CO_2 capture/release we estimated by integrating the current and electrical power vs time (to obtain the charge and energy) and also the CO_2 flow rate vs time (to obtain mols of CO_2) for each electrochemical cycle (Methods). We are able to adjust the charging rate to conserve energy (for example 2.9 GJ per ton_{CO2} at 1 mA cm^{-2}) or increase it for higher kinetics (4 mA cm^{-2}) and a modestly higher 3.4 GJ per ton_{CO2} (Supplementary Fig. 2c). Notably, we observed near-100% release Coulombic efficiency, indicative of the one-electron process for CO_2 release (Supplementary Fig. 2d).

We then used operando Raman spectroscopy in a gas-diffusion-electrode cell under ambient air to investigate the CO_2 capture and release mechanism (Fig. 2c and Supplementary Fig. 3a–c). To simulate the capture process, we scanned the potential from 1.0 V to 0.4 V vs reversible hydrogen electrode (RHE), which correlated with the typical cell voltage we used in capture and release studies (Supplementary Fig. 3d). Bicarbonate (-OCO_2H) characteristic peaks at 1,007 cm^{-1} and 1,376 cm^{-1} (whose identity as -OCO_2H was ascertained by measuring bicarbonate anion reference samples in Supplementary Fig. 4a) were observed once the applied potential descended to 0.7 V: we concluded that MnO_2 surface had begun to reduce and mineralized with CO_2, forming Mn–O–CO_2H. We thus describe 0.7 V as the onset of capture, substantially consistent with the turnover point predicted from the DFT-free energy analysis (Fig. 1e). The peak intensity then progressively increased as we decreased the potential towards ~0.4 V vs RHE (Fig. 2c and Supplementary Fig. 3b), and the carbonate (Mn–OCO_2^-) peak at 1,065 cm^{-1} (assigned based on carbonate anion and $MnCO_3$ reference samples in Supplementary Fig. 4a,e) emerged. We refer this as the capture state, which corresponds to the typical cell voltage of −1 V used in capture and release studies (for example, Fig. 2b) for capturing. It is worth noting that this surface mineralization state is distinct from bulk carbonate formation, as seen in Supplementary Fig. 4e. The potential-dependent change in peak intensity suggests that the -OCO_2H/-OCO_2^- were bound to the surface of the metal oxide. We included a control study (Supplementary Fig. 4b) with no metal oxide and found neither carbonate nor bicarbonate peaks.

We sought to study how the surface is influenced by the presence versus the absence of CO_2. When we exclude CO_2 in the system, we see a feature in Raman at 830 cm^{-1} when the potential is below 0.7 V vs RHE, which we tentatively ascribed to Mn–OH (Supplementary Fig. 4c). To test this assignment, we replaced water with deuterated water and found that the peak shifted to lower wavenumber (630 cm^{-1}): the fact that heavier deuterium shifts the Mn–OH interaction to lower wavenumber is consistent with the picture of hydroxide emerging as the species produced under reducing conditions in the absence of CO_2 (Supplementary Fig. 4d). This is compatible with prior studies in which the MnO_2–MnOOH transition was used to produce solution-phase OH^- for liquid-phase capture and carbonate transport to the anode inside electrochemical capture cells (similar to the pH-swing process depicted in Fig. 1a).

The striking difference relative to this work is that in the presence of CO_2, the CO_2 is adsorbed onto the reduced solid metal oxide sorbent, is not released into solution and thus remains bound for later release from the same side of the electrolyser. This process was corroborated by Raman studies: in the presence of CO_2, the Mn–OH, a characteristic peak of MnOOH, was not observed, and instead a Mn–OCO_2H peak emerged at potentials below 0.7 V vs RHE (Supplementary Fig. 3b,c). Additionally, the Raman spectrum at the capture stated at 0.4 V vs RHE matches well with that of the reference $MnCO_3$ sample at 660, 720 and 1,065 cm^{-1} (Supplementary Fig. 4e). These observations are consistent with the picture in which Mn–O^- provides high nucleophilic reactivity with CO_2 (ref. 14), leading to the formation of surface-mineralized Mn–OCO_2H, replacing Mn–OH when CO_2 is introduced.

We carried out a DFT study based on the δ-phase MnO_2 (Supplementary Fig. 5a) to explore further this concept. Under sufficiently negative potential, the Mn–O^- intermediate will prefer to react with CO_2, forming Mn–OCO_2H, instead of H_2O, a reaction that would form Mn–OH (Supplementary Fig. 5b), an effect also observed in a previous pH-swing study[4]. These findings agree with the operando Raman spectroscopy results, wherein the Mn–OCO_2H peak is observed instead of Mn–OH.

Experimentally we explored the release process by increasing the potential towards +1.0 V. When we employed operando Raman, we saw the reverse of the capture process: the Mn–OCO_2^- peak and the Mn–OCO_2H peak progressively decreased when the potential was scanned from the capture state at 0.4 V to the release state at 1.0 V, at which an equilibrated state that includes the presence of MnO_2 is produced (Fig. 2c and Supplementary Fig. 3c).

Taken together, operando Raman and DFT results point to reversible surface CO_2 mineralization driven by an electrochemical surface redox reaction of manganese dioxide: we propose that CO_2 species are specifically absorbed on the surface of manganese oxide during this pseudo-capacitive process. This is distinct from indirect pH-swing CO_2 capture/release that relies on the chemical reaction between OH^- and CO_2, with its lower bound on energy prescribed by the requisite pH gradient (Fig. 1a–c). This picture in which CO_2 is implicated in the redox cycling of MnO_2 is also suggested by the increase in the redox current density in cyclic voltammetries (CVs) when we increase the CO_2 concentration in the feed gas (Supplementary Fig. 6). Such a trend is similarly seen in quinone-based systems when the carboxylation of the reduced quinone alters the shape of the CV as a function of CO_2 concentration in the feed gas[3,26].

We also studied eCO_2-sMDCR devices in a flue gas capture scenario (Supplementary Fig. 7) using 4% CO_2 (relevant to natural gas combined cycle power plants) balanced with N_2[27]. When we used a high-loading electrode optimized for the flue use case, the eCO_2-sMDCR device simultaneously achieves these performance metrics: a CO_2 capacity and productivity of ~ 300 ton_{CO2} per $ton_{sorbent}$ per year, a single-pass removal depth of 70% and an energy cost of ~ 1.7 GJ per ton_{CO2} for 4% flue gas CO_2 at 50 mA cm^{-2} with good cyclic durability.

Performance evaluation in direct air capture

We then attempted to capture and release CO_2 from air at 0.04% concentration; a task often rendered challenging in general by many materials' sensitivity to oxygen[13,23,28,29]. As an additional challenge, water in ambient air often competes with CO_2 for the active sites and thus adds extra regeneration energy in thermal-regenerated solid-sorbent systems[30].

However, in the present system, we see little evidence of the formation of superoxide—a finding that we attribute to the moderate MnO_2 redox potential at around 0.7 V vs RHE (Fig. 2c). In addition, MnO_2 prefers, as noted above, to react with CO_2 instead of with H_2O.

We therefore introduced air with 0.04% CO_2 and 21% O_2, and we monitored the humidity, observing 20–30% and 60–70% relative humidity at the cell inlet and outlet, respectively (Supplementary Fig. 8a), when we operated the system under a (DAC-relevant) pressure drop of 150 Pa (Supplementary Fig. 8b). To study oxygen tolerance, we compared CVs under said air flow vs N_2 (Supplementary Fig. 8c), finding these to be near-identical, indicating an absence of competing oxygen reduction in the operating voltage range. Then, the DAC performance was evaluated with the charging rate of 1 mA cm^{-2} between −1 V and 1 V, the CO_2 was captured at an increasing capture rate, which reached the maximum of around 0.6 $\mu mol_{capture}$ min^{-1} when the cell voltage

https://doi.org/10.1038/s41560-026-01989-9

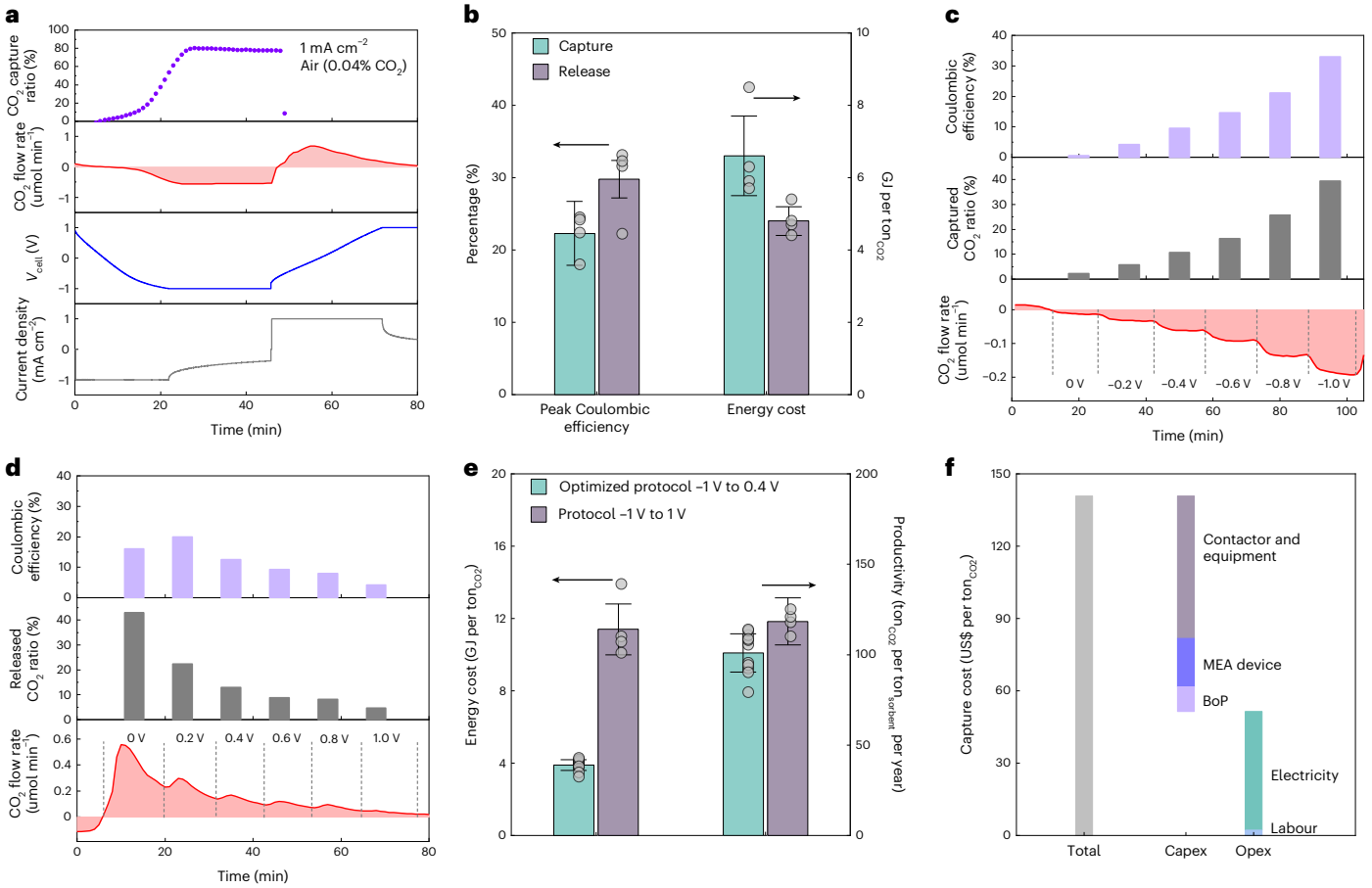

Fig. 3 | Direct air capture performance of eCO$_2$-sMDCR devices. a, The applied electrochemical charging protocol (grey), cell voltage profile (blue), CO_2 molar flow rate (red) and CO_2 capture ratio (purple) in a typical −1 V to 1 V DAC cycle. **b**, Corresponding peak Coulombic efficiency and energy cost for capture and release processes in the −1 V to 1 V DAC cycle. **c**,**d**, Optimization of protocol through tacking the Coulombic efficiency, captured/released ratio in each voltage step and CO_2 molar flow rate with stepped capture (**c**) and release (**d**) at a step of 0.2 V. **e**, Comparison of energy cost and productivity (kinetics) of −1 V to 1 V DAC and optimized −1 V to 0.4 V DAC protocol. **f**, Techno-economic analysis of the levelized cost of carbon capture based on experimentally measured eCO$_2$-sMDCR device performance. In **b** and **e**, the results are presented as averaged values, and error bars represent the standard deviation from at least four independent tests.

approached −1 V (Fig. 3a), leading to a peak CO_2 capture ratio of nearly 80%. Then, when the cell voltage was scanned towards 1 V, a fast CO_2 release was observed with a maximum rate of 0.7 $\mu mol_{capture}\ min^{-1}$ (Fig. 3a). The peak Coulombic efficiency approached 22% and 30% for capture and release, which resulted in energy costs of 6.6 GJ per ton_{CO2} and 4.8 GJ per ton_{CO2} for capture and release, respectively (Fig. 3b). The lower Coulombic efficiency and higher energy cost compared to pure CO_2 (Supplementary Fig. 2d) and flue gas capture (Supplementary Fig. 7d) we attribute to the low concentration of CO_2 in air, which limits contact of CO_2 near the MnO_2 surface over a specific time duration, thus affecting productivity—and the judiciously managed air flow rate, selected to keep projected pressure drop acceptable—these factors leading to parasitic reactions (for example, with H_2O, as seen in Supplementary Fig. 4c).

We then sought to tune the conditions of the capture and release protocol to improve these energetics (Methods). In particular, we sought to optimize the operating voltage window for CO_2 capture and release in a stepped capture and release experiment, which captured CO_2 at −1 V and stepped released CO_2 towards 0.4 V (Fig. 3c,d). This leads to an energy cost of 3.9 GJ per ton_{CO2} for DAC (Fig. 3e, left axis), encouraging in comparison with prior DAC approaches, which were in the 8–10 GJ per ton range[31,32].

We sought to characterize capture and release capacity and kinetics, measuring an estimated capacity of 0.42 mmol g^{-1} and peak capture and release rate of 0.01 and 0.02 $mmol_{CO2}\ g^{-1}\ min^{-1}$, respectively (Supplementary Fig. 10), similar in order to that achieved in typical solid amine sorbents[33,34]. We sought also to test how the energetics when CO_2 is released into a highly concentrated stream; we therefore studied the same air capture process, but released with pure CO_2 as carrier gas (Supplementary Fig. 11). In this configuration, the energy cost was 4.1 GJ per ton_{CO2}, and the CO_2 sorbent capacity was estimated to be 0.41 mmol g^{-1} (Supplementary Fig. 11). We thus use this value to reflect the release performance under a pure CO_2 condition, while also noting that the most practical-relevant case might not involve a carrier gas. Nevertheless, in the techno-economic analysis (TEA), we include estimated additional energy costs for vacuum pumping and compression.

To provide a reference, we tested a widely employed amine sorbent, tetraethylenepentamine (TEPA), loaded in the same porous gas-diffusion media in the same reactor under the same flow conditions. Under dry condition, the performance of the TEPA sorbent in terms of sorbent capacity and productivity is found to be in similar range as the reported values (Supplementary Table 1)[35]. That said, we did find a striking difference when humid air (80 relative humidity (RH%)) was fed to the system: the capture rate was substantially reduced for TEPA sorbent while the rate maintained for e-switching MnO_2 (Supplementary Fig. 12), highlighting the advantage of humidity tolerance of the electrochemical strategy. The active Mn atom utilization was ~4%, consistent with the surface atom ratio; while this surface utilization offers competitive electrode capacity (1.1 mmol

https://doi.org/10.1038/s41560-026-01989-9

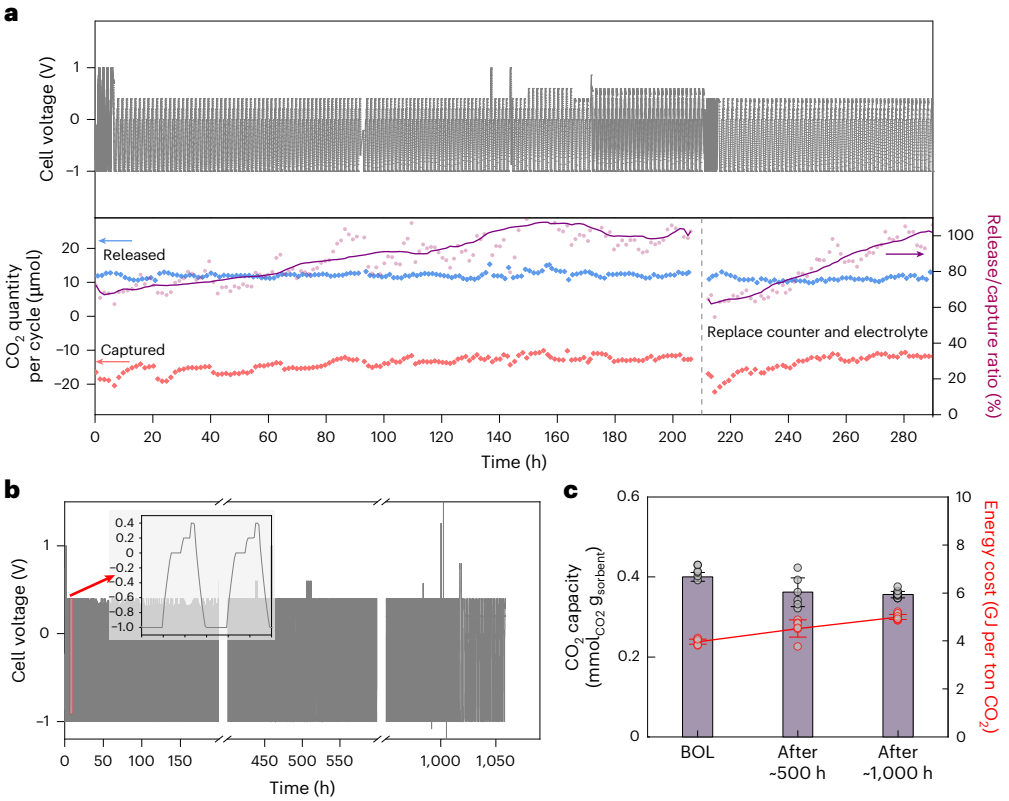

Fig. 4 | Direct air capture durability evaluation of the eCO_2-sMDCR device. The device was subjected to a complete capture and release voltage cycle (around 1.4 hours per cycle) with continuous airflow. **a**, The CO_2 release performance remained stable throughout the 290 hours of the test, while the release-to-capture ratio gradually reached 100%, indicating a balance in carbon mass during stable operation. The replacement of the counter electrode and electrolyte was to evaluate the degradation of the CO_2 capture and release working electrode. **b**, Durability cycling of the device over 1,000 hours. The inset represented the zoom-in of the cyclic voltage profile from −1 V to 0.4 V, while a higher upper voltage was also examined occasionally. The x-axis breaks are in three sections to show the period when the CO_2 capture and release performance was recorded at the begining-of-life (BOL), after around 500 hours and after 1,000 hours; the cycling was continued between these performance tests. **c**, Corresponding capacity of the working electrode and energy cost for the capture+release processes throughout the stability test. In **c**, the results are presented as averaged values, and the error bars represent the standard deviation. The BOL results were obtained from at least four independent tests while the post-stability results were averaged from at least five capture and release test cycles.

per cm^3_{MnO2} vs 0.28 mmol per $cm^3_{solid\text{-}amine}$; Supplementary Table 2), we still note opportunities for further materials engineering (for example, high-surface-area MnO_2 shown in Supplementary Fig. 13) and porous electrode engineering to improve further the volumetric performance of the electro-switched contactor. Notably, this potential-driven electrochemical surface mineralization shows a rate over eight orders of magnitude higher compared to more kinetically limited natural chemical mineralization[36] (~100 vs 1×10^{-6} ton_{CO2} per $ton_{sorbent}$ per year), indicating the high reactivity of $M{-}O^-$ with CO_2. The capture and release kinetics are reflected in the productivity of ~100 ton_{CO2} per ton_{MnO2} per year (Fig. 3e, right axis), which is in a similar regime as sorbent approaches (shown in Supplementary Table 1).

These results lead to an estimated capital cost contribution of US90_{capex}$ per ton_{CO2} when the membrane electrode assembly (MEA) devices are loaded into a laminar contactor structure similar to the solid-sorbent contactor (Fig. 3f, Supplementary Fig. 14 and detail in Supplementary Note 1). Operating cost (dominated by electricity cost) contributes an additional US52_{opex}$ per ton_{CO2} in an analysis of a DAC plant that captures 1 $Mton_{CO2}$ per year (Fig. 3f, Supplementary Fig. 14 and detail in Supplementary Note 1).

Evaluation of durability in direct air capture

A key criterion for DAC application is system durability, which determines the system-lifetime-averaged cost (levelized cost) of the DAC technology. The presence of O_2 poses durability challenges for several organic-based technologies (for example, superoxide formation between reduced quinones and O_2)[12], and these challenges are exacerbated in DAC while the O_2 concentration is over 500 times that of CO_2. The DAC durability of the eCO_2-sMDCR device was evaluated by continuously running complete DAC capture and release cycles (roughly 1.4 hours per cycle). It was found that the eCO_2-sMDCR performance was stable over 200 hours of continuous cycling operation (Fig. 4a), and the oxygen tolerance remained as before (Supplementary Fig. 15). The ratio of CO_2 release and capture reached ~100%, consistent with a picture wherein all captured CO_2 was later released in steady-state cyclic operation. We examined the degradation in CV following continuous voltage cycling and found that this arose due to an increased rate of loss at the electrolyte-immersed and flushed counter electrode. The CV capacitance was fully recovered when the counter electrode was replaced (Supplementary Fig. 16), and the DAC performance was equilibrated and maintained for an additional 100 hours. We note that in a symmetric eCO_2-sMDCR device, the counter electrode is not flushed by electrolyte while it carries out CO_2 capture and release 180° out-of-phase with the working electrode (Supplementary Fig. 17). Structural characterization showed that the major structural features were still preserved (Supplementary Fig. 18). To examine stability, we cycled a device for 1,000 hours and analysed DAC performance (Fig. 4b) every 500 hours. The DAC capacity was retained above 90% of its initial value (Fig. 4c), and the pro-rated relative performance was estimated to be ~92% (Supplementary Fig. 19), and the total capture + release energy cost remained below 5 GJ per ton_{CO2} following operation over 1,000 hours (Fig. 4c and equation (3) in Methods for calculation detail).

Materials and system requirements for scaling

To test initial scalability, we sought to go from 5 cm^2 to 20 cm^2. In the 20 cm^2 device (Supplementary Fig. 20), the sorbent capacity was measured to be 0.57 mmol g^{-1} compared to 0.42 mmol g^{-1} in the 5 cm^2 case, corresponding to an ~1.3× increase in productivity (to 135 $ton_{CO2\,per}$ $ton_{sorbent}$ per year), all with a similar energy cost of 3.4 GJ per ton_{CO2} (Supplementary Fig. 20).

As a preliminary exploration, we studied (Supplementary Fig. 21) the use of capture material at high loading in both counter and working electrodes, where these experiments led to 1,230 umol of CO_2 separated per cycle in the 20 cm^2 high-loading device, nearly two orders of magnitude increase from the previously demonstrated value from a 5 cm^2 device. We portray a laminar unit and contactor arrays of a potential future configuration in Supplementary Fig. 22 and Supplementary Table 2, drawing analogy with representative commercial demonstration pilot plants[37].

We point out important areas of future research, including management of gas, electrolyte, pressure drop, volumetric productivity and CO_2 purity in future scaled systems. Future studies can include exploration of stable, high-surface-area materials; mechanically self-supported electrode-current collector architectures to strengthen the laminar scaffold and solid-state electrolyte systems that offer to reduce the complexity of electrolyte management and address the issue of evaporative loss.

Conclusion

The performance of eCO_2-sMDCR devices and the mechanistic picture elaborated using operando Raman spectroscopy suggest an inorganic electrochemical pathway to contribute to addressing the combined challenge of cost, energy consumption and durability in carbon capture, particularly direct air capture. The eCO_2-sMDCR device can, by its driving voltage profile in time, be tailored to different CO_2 capture and release scenarios.

Methods

Materials

Manganese(II) sulfate monohydrate (ReagentPlus, ≥99%), potassium permanganate (ACS reagent, ≥99.0%), sodium sulfate (ACS reagent, ≥99.0%, anhydrous, powder), sodium phosphate dibasic (ACS reagent, ≥99.0%), sodium hydroxide (puriss, 98-100.5%), potassium hydroxide (ACS reagent, ≥85%), gold(III) chloride trihydrate (> 99.9%), citric acid (> 99.0%), methanol (99.8%), were all purchased from Sigma-Aldrich without further treatment. Freudenberg H23C3, H23 graphite felt (GF020), carbon black (Vulcan XC72) and a Piperion membrane (40 μm) were purchased from Fuel Cell Store. Nafion perfluorinated resin solution (D520), Nafion 212, Nafion 117 membrane were purchased from Ion power. PP separators (Celgard 3400) were purchased from Celgard. The Ag/AgCl reference electrodes used in the flow cell were purchased from CHI Instruments Inc. Gaseous CO_2 (research grade), N_2 (ultra-high purity) and Ar (ultra-high purity) were purchased from Airgas. Ultra-pure water (18.2 MΩ from MilliQ) was used to prepare all the solutions and electrolytes.

Synthesis of MnO_2

To synthesize the MnO_2, 120 ml 0.2 mol l^{-1} $MnSO_4$ solution was mixed with 80 ml 0.2 mol l^{-1} $KMnO_4$ solution under stirring in a 325 ml glass vial. The mixture was then stirred for 30 min at room temperature. The brown MnO_2 precipitate was then collected by centrifugation, washed several times with water and dried under vacuum.

Synthesis of 55 nm Au@MnO_2 NPs for surface-enhanced Raman spectroscopy tests

Au nanoparticles (NPs) were synthesized by adding 2.537 ml of a 0.863 wt% $HAuCl_4$ aqueous solution into 200 ml of ultra-pure water in a 250 ml round-bottom flask. The solution was then heated to a boil, followed by the addition of 1.5 ml 1% citric acid (CA) solution. Then, the mixture continued boiling for 30 minutes and was cooled naturally to obtain the Au NPs solution.

Au@MnO_2 core-shell nanoparticle was then synthesized by taking 10 ml of the prepared Au NPs solution and adding 170 ml of 0.1 M KOH, 0.5 ml of 0.01 M $KMnO_4$ and 2.5 ml of 0.01 M $MnSO_4$ or $K_2C_2O_4$ as a reducing agent. The mixture was then placed in an ice bath for 60 minutes to ensure complete reaction.

Electrode preparation

To prepare the electrodes used in the membrane-electrode assembly (MEA) device, 300 mg of synthesized MnO_2, 30 mg of carbon black, 15 ml of methanol and 600 mg of 5 wt% Nafion solution were added into a 40 ml vial. The mixture was sealed and sonicated in a water bath for 2 hours at room temperature. The solution was then sprayed onto a 5 cm × 5 cm gas-diffusion electrode (Freudenberg H23C3 for the working electrode and H23 for the counter electrode). The final material loading was controlled to be ~10 mg cm^{-2}, and the MnO_2 sorbent loading was estimated to be ~83 wt% based on the ink composition. After drying, the gas-diffusion electrode was cut into four 5 cm^2 pieces for further use. The high-loading 70 mg cm^{-2} electrodes were prepared with a similar ink composition but with a simple dip-coating approach. Specifically, 700 mg of synthesized MnO_2, 70 mg of carbon black, 30 ml of methanol and 1,400 mg of 5% Nafion solution were added and sonicated in a 40 ml vial. Two 5 cm^2 graphite felt were immersed into the ink, followed by vacuum drying repeatedly until all the materials were loaded into the graphite felt. The final catalyst loading was measured to be ~ 70 mg cm^{-2}.

CO_2 capture and release device assembly

To fabricate the electrified CO_2 surface mineralization/demineralization capture/release (eCO_2-sMDCR) device, two pieces of 5 cm^2 MnO_2-coated electrodes were pressed onto a membrane separator. The hydrophobic-coated H23C3 was used as the working electrode contacting with gases, and the coated H23 was used as the counter electrode in contact with the aqueous electrolyte. Two sets of silicone rubber gaskets (0.01 inch) with a 5 cm^2 opening were placed between the membrane-electrode assembly and the titanium current collector plates to prevent gas and liquid leakage. The electrolyte (0.5 M Na_2SO_4, buffered by Na_2HPO_4) was pumped to the counter electrode side through a peristaltic pump at around 5 ml min^{-1}. The 20 cm^2 device was assembled following the same protocol as the 5 cm^2 device. The 20 cm^2 symmetric high-loading device was assembled similarly except that the graphite felts were used for the working and counter electrodes, and the electrolyte was fed between the two electrodes.

Electrochemical measurement

Electrochemical measurements were all conducted using a BioLogic VSP300 potentiostat. Gases (N_2, CO_2, house air) were supplied to the working electrode by a mass flow controller (Alicat Scientific). The gas flow was controlled to be a low flow rate of around 30 sccm for air and around 10 sccm for flue gas since a high flow rate would result in a high pressure drop in the practical gas contactor, which would cost a considerable amount of fan energy, particularly in the direct air capture scenario. The pressure drop through the device was measured by a differential pressure gauge. The change of pressure during the electrochemical testing was monitored in separate tests using a pressure transducer (Alicat Scientific) with the inlet and outlet valves closed. The concentration of the CO_2 from the outlet of the device was measured by a CO_2 analyser (T360M, Teledyne and WMA-5 PPSystems). To sustain the required gas-flow rate (> 700 ml min^{-1}) for the CO_2 analyser, the gas flow from the device outlet was diluted with Ar flow (~ 690 sccm) to ensure sufficient gas supply. Before testing, the CO_2 analyser was calibrated with Ar UHP to set the zero point and with diluted CO_2 to check the accuracy of concentration measurement.

The concentration of CO_2 in the house air was measured to be around 435 ppm. The pH of the electrolyte was monitored by a pH meter (Oakton PC450), and the pH was buffered to be around 7 (neutral condition). For device activation, cyclic voltammetry experiments were conducted between −1 V and 1 V at 10 mV s^{-1} and 50 mV s^{-1} under stabilization. For the CO_2 capture and release protocol, the device was charged and discharged at various constant current densities (typically 1 mA cm^{-2}) until the cell voltage reached the set values and held at the set values for a set period of time. Stepped capture and release experiments were conducted, in which the cell voltage was scanned and held every 0.2 V between −1 V and 1 V. The optimized voltage window was selected based on the averaged coulombic efficiency and the CO_2 capture/release capacity. All voltages in device performance testing were reported in full-cell voltage without any iR compensation. The potential applied to the working electrode of the device was probed with an Ag/AgCl (saturated KCl) electrode (0.197 V vs the standard hydrogen electrode) and then converted to the reversible hydrogen electrode using the Nernst equation to correlate with the operando Raman tests.

CO_2 capture and release measurement

The amount of CO_2 being captured or released during an electrochemical cycle can be calculated by integrating the CO_2 flow rate corresponding to the capture or release cycle. The CO_2 capture ratio can be calculated as the ratio of the measured CO_2 concentration during capture to the baseline CO_2 concentration (for example, 435 ppm for air). The CO_2 flow rate can be calculated by the CO_2 concentration difference between the measured value and the baseline concentration of the supplied gas (equation (1)). $c_{CO2,\,measure}$ is the concentration of CO_2 in the gas flow into the analyser, $c_{CO2,\,baseline}$ is the concentration of CO_2 in the feeding gas to the device and the $f_{analyser}$ is the flow rate supplied to the analyser. The conversion from volumetric flow rate (l min^{-1}) to molar flow rate (mol min^{-1}) is calculated by the ideal gas law. The CO_2 removal depth (capture ratio) is calculated by the ratio of $c_{CO2,\,measured}$ and $c_{CO2,\,baseline}$.

$$\mathrm{CO_2\ flow\ rate}\left(\frac{\mathrm{mol}}{\mathrm{min}}\right) = \left\{c_{\mathrm{CO2,\,measure}} - c_{\mathrm{CO2,\,baseline}}\right\}(\%) \times f_{\mathrm{analyser}}\left(\frac{\mathrm{l}}{\mathrm{min}}\right) \times \frac{101\,(\mathrm{kPa})}{8.314\,(\mathrm{J\,(mol\,K)^{-1}}) \times 293.15\,(\mathrm{K})} \quad (1)$$

The Coulombic efficiency (equation (2)) and energy cost (equation (3)) can then be obtained by calculating the quantity of CO_2 from the initial point (t_i) to the final point (t_f) with the corresponding charge (Q) and energy (E) of the electrochemical process. F is the Faradaic constant. Note that the energy cost here only considers the electric work associated with the electrochemical protocol, an additional electric work of 1–2 GJ per ton_{CO2} (ref. 38) might be required for the vacuum pumping and compression processes in the practical application.

$$\text{Columbic efficiency}\,(\%) = \frac{\int_{t_i}^{t_f} \mathrm{CO_2\ flow\ rate} \times \mathrm{d}t \times F}{Q} \quad (2)$$

$$\text{Energy cost}\ (\mathrm{GJ\ per\ ton_{CO2}}) = \frac{E}{\int_{t_i}^{t_f} \mathrm{CO_2\ flow\ rate} \times \mathrm{d}t} \quad (3)$$

The mass-specific or area-specific productivity that reflects the capture and release kinetics was calculated by normalizing the amount of CO_2 released in a complete cycle by the weight of the applied sorbent materials ($w_{sorbent}$) or the active geometric area of the cell (A_{geo}) and the duration of the complete capture and release cycle (t_{cycle}), as shown in equations (4) and (5), respectively.

$$\text{Mass specific productivity}\ (\mathrm{ton_{CO2}\ per\ ton_{sorbent}\ yr^{-1}}) = \frac{\int_{t_i}^{t_f} \mathrm{CO_2\ flow\ rate} \times \mathrm{d}t}{w_{\mathrm{sorbent}}\, t_{\mathrm{cycle}}} \quad (4)$$

$$\text{Area}-\text{specific productivity}\ (\mathrm{ton_{CO2}\ per\ ton_{sorbent}\ yr^{-1}}) = \frac{\int_{t_i}^{t_f} \mathrm{CO_2\ flow\ rate} \times \mathrm{d}t}{A_{\mathrm{geo}}\, t_{\mathrm{cycle}}} \quad (5)$$

For example, the mass-specific productivity under DAC conditions, which captured 15.2 µmol CO_2 per cycle with a total cycling time of 1.4 h, a MnO_2 electrode loading of 41.5 mg and continuous cycling throughout the year, was calculated as shown in equation (6):

$$\frac{15.2\times10^{-6}\ \mathrm{mol\ per\ cycle}}{41.5\times10^{-3}\ \mathrm{g_{MnO2}} \times 1.4\ \mathrm{h\ per\ cycle}} \times \left(44\,\frac{\mathrm{g}}{\mathrm{mol}}\right) \times \left(365\times24\,\frac{\mathrm{h}}{\mathrm{year}}\right) = 101\ (\mathrm{ton_{CO2}\ per\ ton_{sorbent}\,yr^{-1}}) \quad (6)$$

Similarly, the productivity at 50 mA/cm^2 under 4% flue gas condition was calculated in equation (7):

$$\frac{462\times10^{-6}\ \mathrm{mol\ per\ cycle}}{290.5\times10^{-3}\mathrm{g_{MnO2}} \times 1.7\ \mathrm{h\ per\ cycle}} \times \left(44\,\frac{\mathrm{g}}{\mathrm{mol}}\right) \times \left(365\times24\,\frac{\mathrm{h}}{\mathrm{year}}\right) = 356\ (\mathrm{ton_{CO2}\ per\ ton_{sorbent}\ yr^{-1}}) \quad (7)$$

Release into pure CO_2 stream

The direct air capture followed by release into a pure CO_2 carrier gas stream was evaluated by conducting same air capture process, followed by switching the carrier gas into pure CO_2 (2 sccm). Before switching the cell voltage to initiate a release event, a stable CO_2 concentration baseline was established by mixing the pure CO_2 carrier gas from the cell outlet with pure N_2 (300 sccm) for precisely measuring release rate into pure CO_2 using CO_2 analyser (WMA-5 PPSystems). After the CO_2 baseline concentration was stabilized, we started the release programme, monitored the change in CO_2 concentration as a result of the additional CO_2 released into the pure CO_2 carrier gas stream and quantified the release rate and performance metrics using equation (1). The purity of gas during release event was analysed by gas chromatography (Shimadzu).

DAC electrochemical protocol optimization

We evaluated the impact of charging rate on the CO_2 capture and release efficiency and energetics. When we lower the charging rate to 0.5 mA cm^{-2} from 1.0 mA cm^{-2}, the energy cost decreases to 12 GJ ton^{-1} (Supplementary Fig. 9a–c). However, in light of our capital cost estimates, we kept productivity at 1.0 mA cm^{-2}, which had already enabled an over 70% CO_2 capture ratio (Fig. 3b).

The optimum operating voltage window was probed for CO_2 capture and release in a stepped capture and release experiment (Fig. 3c,d). By analysing the corresponding CO_2 capture/release quantities, charges and energy for each step, we are able to determine the optimum capture and release voltage and duration. Interestingly, it was found that the average capture Coulombic reached a maximum of 33% when held at −1 V, and this contributed 40% of the total captured CO_2 quantity (Fig. 3c). The peak release coulombic efficiency of 20% was achieved at 0.2 V, while 80% of CO_2 is released at 0.4 V (Fig. 3d). On the basis of these results, an optimized CO_2 capture and release protocol was derived, which captured CO_2 at −1 V and stepped released CO_2 towards 0.4 V.

Materials characterization

The transmission electron microscopy (TEM) images were taken from a JEOL GrandArm 200 microscope at an acceleration voltage of 200 kV. A probe convergence angle of 20 mrad was used. The XRD measurements were conducted on a STOE STADI MP diffractometer using Mo

or Ag K-α radiation (λ_{Ag} = 0.056 nm, λ_{Mo} = 0.071 nm) to avoid Mn fluorescence; the 2θ value was converted to one based on Cu K-α radiation (λ_{Cu} = 0.154 nm) to be compared with the reference.

Operando Raman spectroscopy

The operando electrochemical surface-enhanced Raman spectroscopy (SERS) measurements were carried out using a PGSTAT204 electrochemical workstation coupled with a RENISHAW inVia confocal Raman microscope. The wavelength utilized in the experiment was 633 nm. A custom-designed Raman cell was employed, featuring a platinum wire as the counter electrode and an Ag/AgCl electrode as the reference electrode (0.197 V vs the standard hydrogen electrode). Core-shell Au@MnO_2 nanoparticles were coated on carbon paper and used as the working electrode.

DFT calculations

Density Functional Theory calculations were performed using the Vienna Ab initio Simulation Package version 6.3.2 (ref. 39) (VASP) and JDFTx[40]. Structural optimizations were performed in VASP and featured the Perdew–Burke–Ernzerhof (PBE) functional[41]. Grimme's D3BJ empirical correction[42] for London Dispersion forces were also included. All atoms were described using Projector Augmented Wave (PAW) pseudopotentials[43] with a global planewave energy cut-off of 520 eV. To avoid antiferromagnetic states, all calculations featured polarized spins, with the initial magnetic moments all aligned to a high spin. The wavefunction convergence criterion was set to $1E^{-6}$ eV, and the force convergence criterion was set to $1E^{-2}$ eV $Å^{-1}$. All calculations used a gamma-centred 3 × 3 × 1 K point grid. VASP was also used to compute phonons to predict thermochemical properties, namely zero-point energies, enthalpies (*H*) and entropies (*S*). Gibbs free energies (*G*) were then computed according to $G = H - TS$, where temperature (*T*) was set to 298.15 K. A detailed discussion of the DFT calculation and the analysis of adsorption structure is included in Supplementary Note 2.

Following structural optimizations, Joint density-functional theory (JDFTx) was used for computing high-accuracy solvation energies. Solvation energy calculations utilized the charge-asymmetric nonlocally determined local-electric (CANDLE) implicit solvation model[44] with solvent parameters matching those of liquid water. Coulomb energies were tapered in the direction orthogonal to the slab surface to eliminate artefactual interaction of the slab with itself in periodic images.

Data availability

The authors declare that all data supporting the major findings are available in the main text or the Supplementary Information. Source data are provided with this paper.

References

1. *Direct Air Capture 2022* (IEA, 2022).
2. Net Zero by 2050 (IEA, 2021).
3. Voskian, S. & Hatton, T. A. Faradaic electro-swing reactive adsorption for CO_2 capture. *Energy Environ. Sci.* **12**, 3530–3547 (2019).
4. Rahimi, M. et al. Carbon dioxide capture using an electrochemically driven proton concentration process. *Cell Rep. Phys. Sci.***1**, 100033 (2020).
5. Sabatino, F., Gazzani, M., Gallucci, F. & van Sint Annaland, M. Modeling, optimization, and techno-economic analysis of bipolar membrane electrodialysis for direct air capture processes. *Ind. Eng. Chem. Res.* **61**, 12668–12679 (2022).
6. Seo, H., Rahimi, M. & Hatton, T. A. Electrochemical carbon dioxide capture and release with a redox-active amine. *J. Am. Chem. Soc.* **144**, 2164–2170 (2022).
7. Pang, S. et al. A phenazine-based high-capacity and high-stability electrochemical CO_2 capture cell with coupled electricity storage. *Nat. Energy* **8**, 1126–1136 (2023).
8. Jin, S., Wu, M., Gordon, R. G., Aziz, M. J. & Kwabi, D. G. pH swing cycle for CO_2 capture electrochemically driven through proton-coupled electron transfer. *Energy Environ. Sci.* **13**, 3706–3722 (2020).
9. Huebscher, R. G. & Babinsky, A. D. Electrochemical concentration and separation of carbon dioxide for advanced life support systems—carbonation cell system. *SAE Trans.* **78**, 2164–2170 (1969).
10. Zhu, P. et al. Continuous carbon capture in an electrochemical solid-electrolyte reactor. *Nature* **618**, 959–966 (2023).
11. Vermaas, D. A., Wiegman, S., Nagaki, T. & Smith, W. A. Ion transport mechanisms in bipolar membranes for (photo) electrochemical water splitting. *Sustain. Energy Fuels* **2**, 2006–2015 (2018).
12. Liu, Y., Ye, H.-Z., Diederichsen, K. M., Van Voorhis, T. & Hatton, T. A. Electrochemically mediated carbon dioxide separation with quinone chemistry in salt-concentrated aqueous media. *Nat. Commun.* **11**, 2278 (2020).
13. Jeziorek, D. et al. Theoretical and electrochemical study of the mechanism of anthraquinone-mediated one-electron reduction of oxygen: the involvement of adducts of dioxygen species to anthraquinones. *J. Chem. Soc. Perkin Trans.* **2**, 229–236 (1997).
14. Lindskog, S. Structure and mechanism of carbonic anhydrase. *Pharmacol. Ther.* **74**, 1–20 (1997).
15. Wilcox, J. *Carbon Capture* (Springer Science & Business Media, 2012).
16. Singh, A. K. et al. Electrochemical stability of metastable materials. *Chem. Mater.* **29**, 10159–10167 (2017).
17. Persson, K. A., Waldwick, B., Lazic, P. & Ceder, G. Prediction of solid-aqueous equilibria: scheme to combine first-principles calculations of solids with experimental aqueous states. *Phys. Rev. B* **85**, 235438 (2012).
18. Jain, A. et al. Commentary: the materials project: a materials genome approach to accelerating materials innovation. *APL Mater.* **1**, 011002 (2013).
19. Patel, A. M., Nørskov, J. K., Persson, K. A. & Montoya, J. H. Efficient Pourbaix diagrams of many-element compounds. *Phys. Chem. Chem. Phys.* **21**, 25323–25327 (2019).
20. Drage, T. C. et al. Materials challenges for the development of solid sorbents for post-combustion carbon capture. *J. Mater. Chem.* **22**, 2815–2823 (2012).
21. Min, Y. J., Ganesan, A., Realff, M. J. & Jones, C. W. Direct air capture of CO_2 using poly(ethyleneimine)-functionalized expanded poly(tetrafluoroethylene)/silica composite structured sorbents. *ACS Appl. Mater. Interfaces* **14**, 40992–41002 (2022).
22. Li, H. et al. Capturing carbon dioxide from air with charged-sorbents. *Nature* **630**, 654–659 (2024).
23. Seo, H. & Hatton, T. A. Electrochemical direct air capture of CO_2 using neutral red as reversible redox-active material. *Nat. Commun.* **14**, 313 (2023).
24. Zhou, Z. et al. Carbon dioxide capture from open air using covalent organic frameworks. *Nature* **635**, 96–101 (2024).
25. Boualavong, J., Gorski, C. A. & Liu, Y. Translatable reporting of energy demand and rates in electrochemical carbon capture. *iScience* **28**, 111781 (2025).
26. Simeon, F. et al. Electrochemical and molecular assessment of quinones as CO_2-binding redox molecules for carbon capture. *J. Phys. Chem. C* **126**, 1389–1399 (2022).
27. Wang, X. & Song, C. Carbon capture from flue gas and the atmosphere: a perspective. *Front. Energy Res.* https://doi.org/10.3389/fenrg.2020.560849 (2020).
28. Socolow, R. et al. *Direct Air Capture of CO_2 with Chemicals: A Technology Assessment for the APS Panel on Public Affairs* (American Physical Society, 2011).

29. Barlow, J. M. & Yang, J. Y. Oxygen-stable electrochemical CO_2 capture and concentration with quinones using alcohol additives. *J. Am. Chem. Soc.* **144**, 14161–14169 (2022).
30. Wiegner, J. F., Grimm, A., Weimann, L. & Gazzani, M. Optimal design and operation of solid sorbent direct air capture processes at varying ambient conditions. *Ind. Eng. Chem. Res.* **61**, 12649–12667 (2022).
31. Keith, D. W., Holmes, G., St. Angelo, D. & Heidel, K. A process for capturing CO_2 from the atmosphere. *Joule* **2**, 1573–1594 (2018).
32. Wurzbacher, J. A., Gebald, C., Brunner, S. & Steinfeld, A. Heat and mass transfer of temperature–vacuum swing desorption for CO_2 capture from air. *Chem. Eng. J.* **283**, 1329–1338 (2016).
33. Choi, S., Gray, M. L. & Jones, C. W. Amine-tethered solid adsorbents coupling high adsorption capacity and regenerability for CO_2 capture from ambient air. *ChemSusChem* **4**, 628–635 (2011).
34. Shi, X., Lin, Y. & Chen, X. Development of sorbent materials for direct air capture of CO_2. *MRS Bull.* **47**, 405–415 (2022).
35. Song, M. et al. Amine-functionalized MIL-101(Cr) fibers for direct air capture at cold temperatures using rapid temperature vacuum swing adsorption. *Chem. Eng. J.* **477**, 147135 (2023).
36. Rahimi, M., Khurram, A., Hatton, T. A. & Gallant, B. Electrochemical carbon capture processes for mitigation of CO_2 emissions. *Chem. Soc. Rev.* **51**, 8676–8695 (2022).
37. Spiteri, A., Megerle, B., Calbry-Muzyka, A., Casas, N. & Wurzbacher, J. A. Method for capture of carbon dioxide from ambient air and corresponding adsorber structures with a plurality of parallel surfaces. US patent WO2021239747A1 (2021).
38. Ozkan, M. Atmospheric alchemy: the energy and cost dynamics of direct air carbon capture. *MRS Energy Sustain.* **12**, 46–61 (2025).
39. Kresse, G. & Furthmüller, J. Efficiency of ab-initio total energy calculations for metals and semiconductors using a plane-wave basis set. *Comput. Mater. Sci.* **6**, 15–50 (1996).
40. Sundararaman, R. et al. JDFTx: software for joint density-functional theory. *SoftwareX* **6**, 278–284 (2017).
41. Perdew, J. P., Burke, K. & Ernzerhof, M. Generalized gradient approximation made simple. *Phys. Rev. Lett.* **77**, 3865–3868 (1996).
42. Grimme, S., Antony, J., Ehrlich, S. & Krieg, H. A consistent and accurate ab initio parametrization of density functional dispersion correction (DFT-D) for the 94 elements H-Pu. *J. Chem. Phys.* **132**, 154104 (2010).
43. Kresse, G. & Joubert, D. From ultrasoft pseudopotentials to the projector augmented-wave method. *Phys. Rev. B* **59**, 1758–1775 (1999).
44. Sundararaman, R. & Goddard, W. A. III. The charge-asymmetric nonlocally determined local-electric (CANDLE) solvation model. *J. Chem. Phys.* **142**, 064107 (2015).
45. Momma, K. & Izumi, F. VESTA 3 for three-dimensional visualization of crystal, volumetric and morphology data. *J. Appl. Crystallogr.* **44**, 1272–1276 (2011).

Acknowledgements

This work made use of the Northwestern University Micro/Nano Fabrication Facility (NUFAB) facility of Northwestern University's Atomic and Nanoscale Characterization Experimental Center (NUANCE), which has received support from the Soft and Hybrid Nanotechnology Experimental (SHyNE) Resource (National Science Foundation, NSF ECCS-2025633), the International Institute for Nanotechnology (IIN) and Northwestern's Materials Research Science and Engineering Center (MRSEC) programme (NSF DMR-2308691). W.A.G. thanks Department of Energy (DOE) (SC-0022230) for support. DFT calculations were also supported through computational resources and staff contributions provided for the Quest high-performance computing facility at Northwestern University, which is jointly supported by the Office of the Provost, the Office of Research and Northwestern University Information Technology. Funding: this work was financially supported by TotalEnergies SE.

Author contributions

Conceptualization: K.X., E.H.S., Z.L. and B.P. Materials synthesis, device development, testing methodology development and experimental validation: Z.L. and B.P. Materials structural characterization: B.P. Raman experiments design, measurement and interpretation: H.Z. Simulation studies: C.B.M. Adsorption isotherm characterization: M.K.S. Supplementary three-electrode investigations: Z.L., H.S.J. and H.L. Supervision: W.A.G., K.O.K., O.K.F., K.X. and E.H.S. Funding acquisition: O.K.F. and E.H.S. Writing–original draft: Z.L., B.P. and H.Z. Writing–reviewing and editing: Z.L., B.P., M.K.S., H.L., K.O.K, O.K.F., K.X. and E.H.S.

Competing interests

Z.L., K.X. and E.H.S. are filling a patent based on this work. The remaining authors declare no competing interests.

Additional information

Supplementary information The online version contains supplementary material available at https://doi.org/10.1038/s41560-026-01989-9.

Correspondence and requests for materials should be addressed to Ke Xie or Edward H. Sargent.

Peer review information *Nature Energy* thanks the anonymous reviewers for their contribution to the peer review of this work.